

Nanoscale

Accepted Manuscript



This is an *Accepted Manuscript*, which has been through the Royal Society of Chemistry peer review process and has been accepted for publication.

Accepted Manuscripts are published online shortly after acceptance, before technical editing, formatting and proof reading. Using this free service, authors can make their results available to the community, in citable form, before we publish the edited article. We will replace this *Accepted Manuscript* with the edited and formatted *Advance Article* as soon as it is available.

You can find more information about *Accepted Manuscripts* in the [Information for Authors](#).

Please note that technical editing may introduce minor changes to the text and/or graphics, which may alter content. The journal's standard [Terms & Conditions](#) and the [Ethical guidelines](#) still apply. In no event shall the Royal Society of Chemistry be held responsible for any errors or omissions in this *Accepted Manuscript* or any consequences arising from the use of any information it contains.

ARTICLE

Defective TiO₂-supported Cu nanoparticles as efficient and stable electrocatalysts for oxygen reduction in alkaline media

Cite this: DOI: 10.1039/x0xx00000x

Ke Liu, Yang Song, and Shaowei Chen*

Received 00th January 2012,

Accepted 00th January 2012

DOI: 10.1039/x0xx00000x

www.rsc.org/

Nanocomposites based on TiO₂-supported copper nanoparticles were prepared by a hydrothermal method where copper nanoparticles with or without the passivation of 1-decyne were chemically grown onto TiO₂ nanocolloid surfaces (and hence denoted as CuHC10/TiO₂ and Cu/TiO₂, respectively). Transmission electron microscopic measurements showed that the size of the hybrid nanoparticles was 5 to 15 nm in diameter with clearly-defined lattice fringes for anatase TiO₂(101) and Cu(111). The formation of anatase TiO₂ nanoparticles was also observed in X-ray diffraction measurements. FTIR measurements confirmed successful attachment of alkyne ligands onto the surface of the copper nanoparticles via Cu–C≡ interfacial bonds in CuHC10/TiO₂. XPS measurements suggested the formation of CuO in both samples with a higher concentration in Cu/TiO₂; and interestingly, Ti³⁺ species were found in CuHC10/TiO₂ but absent in Cu/TiO₂ or TiO₂ nanoparticles. Electrochemical studies demonstrated that both Cu/TiO₂ and CuHC10/TiO₂ exhibited a markedly improved electrocatalytic performance in oxygen reduction reaction, as compared to that of TiO₂ nanocolloids alone, within the context of onset potential, number of electron transfer involved and kinetic current density. Importantly, among the series, CuHC10/TiO₂ exhibited the best ORR activity with a high current density, an almost four-electron reduction pathway and long-term stability after 4000 cycles at high potentials, which may be ascribed to the defective TiO₂ structures in combination with surface ligand engineering.

1. Introduction

Proton exchange membrane fuel cells (PEMFC) are clean, efficient and environmental-friendly electrochemical power generators.¹ However, the sluggish kinetics of oxygen reduction reaction (ORR) at the cathode represents one of the greatest challenges in the wide-spread commercialization of PEMFC. Carbon-supported platinum-based nanoparticle catalysts have been extensively used for fuel cell electrodes;²⁻⁴ yet further improvement of their performance is urgently needed due to the scarcity and high costs of platinum. In fact, a variety of strategies have been developed to improve the ORR activities, such as preparation of Pt-based alloys⁵ and surface functionalization of Pt nanoparticles with selected organic ligands.⁶⁻⁸ An alternative approach is to replace Pt with earth-abundant non-precious materials.⁹ Among these, little attention has been paid to copper-based electrocatalysts although copper is inexpensive and abundant with remarkable conductivity.¹⁰⁻¹² In fact, copper has been used extensively as supporting or non-active components in oxygen reduction reactions,¹³⁻¹⁵ although ORR activities of poly- or single-crystalline bulk copper has

been reported in the literature in a borax buffer solution^{16, 17} or in sulfuric acid solution.¹⁸ More recently, it has been shown that the ORR activity might be markedly enhanced with alkyne-capped nanosized copper particles,¹⁹ suggesting that copper, when properly engineered, might be a viable material for ORR electrocatalysis.

Note that metal nanoparticle catalysts are usually dispersed on substrates of high surface areas and/or good conductivity. Of these, carbon black is one of the most commonly used catalyst supports in oxygen reduction reaction due to high surface area and good electronic conductivity.^{20, 21} However, oxidation of carbon supports at potentials higher than +0.9 V vs RHE causes degradation in catalyst performance during fuel cell operation.²² Therefore, it is important to identify oxidation-resistant catalyst supports to meet the durability requirements of PEMFC catalysts. Titanium dioxide has been regarded as an attractive support for ORR catalysts due to its low costs, abundance, and long-term chemical stability in extreme conditions. In addition, the hypo-d-electron nature of titanium dioxide enables strong metal-support interactions,^{23, 24} leading to enhanced dispersion

of catalyst nanoparticles and improved catalytic activities. In fact, it has been reported that platinum nanoparticles supported on TiO₂ nanoparticles possessed a greater surface area²⁵ and a higher ORR activity than commercial Pt/C,²⁶ and PtPd/TiO₂ nanocomposite electrocatalysts showed activity comparable to that of Pt/C with enhanced stability at high potentials.²⁷ Therefore, TiO₂ appears to be a promising alternative for ORR catalyst support.²⁸ This is the primary motivation of the present study where we examine the ORR activity of nanocomposites based on copper nanoparticles supported on TiO₂ nanocolloids.

Herein anatase TiO₂ nanocolloids were prepared by the hydrolysis of titanium(IV) n-butoxide with the assistance of chloroaniline and oleic acid via hydrothermal treatments. Then copper nanoparticles were chemically grown on TiO₂ nanocolloids by simple sodium borohydride reduction, as manifested in TEM and XRD measurements. FTIR measurements confirmed successful attachment of the alkyne ligands onto the nanoparticle surface in CuHC10/TiO₂ possibly by the formation of Cu–C≡ interfacial bonds. XPS measurements revealed that CuO species were formed in the nanocomposites with the concentration higher in Cu/TiO₂ than in CuHC10/TiO₂. Interestingly, Ti(III) species were identified in CuHC10/TiO₂ but absent in Cu/TiO₂, which was believed to be beneficial to the electronic conductivity of the TiO₂ supports.²⁹ Electrochemical studies indicated that oxygen reduction reaction proceeded mainly via the 4e pathway on both Cu/TiO₂ and CuHC10/TiO₂ samples as compared to the 2e pathway at TiO₂ nanoparticles alone. Excellent long-term stability was also retained for the nanocomposite catalysts after 4000 cycles at high potentials, and CuHC10/TiO₂ samples stood out as the best catalysts among the series, likely the combined results of defective support and surface ligand engineering.

2. Experimental Section

2.1 Chemicals

3-Chloroaniline (99%, ACROS), titanium(IV) n-butoxide (99%, ACROS), oleic acid (Fisher Scientific), Nafion® 117 solution (Fluka), copper acetate (Cu(OAc)₂·H₂O, 99.9%, Alfa Aesar), 1-decyne (HC10, TCI America), and sodium borohydride (NaBH₄, ≥98%, ACROS) were all used as received. Solvents were purchased at the highest purity available from typical commercial sources and also used without further treatment. Water was deionized with a Barnstead Nanopure water system (18.3 MΩ·cm). Ultrapure N₂ and O₂ were used for the deaeration of the electrolyte solutions and oxygen reduction reactions, respectively.

2.2 Preparation of TiO₂ supported Cu nanoparticles

TiO₂ nanoparticles were prepared by following a literature procedure.³⁰ In a typical reaction, 0.05 mL of 3-chloroaniline was added into 5 mL of Nanopure water and then transferred to a Teflon-lined stainless-steel autoclave. Meanwhile, 0.085 g of titanium(IV) n-butoxide and 0.5 mL of oleic acid were

dissolved in 5 mL of toluene and also transferred to the autoclave. The mixed solution was subject to hydrothermal treatments at 180 °C for 12 h, and the as-obtained white precipitates (TiO₂) were collected and rinsed extensively with methanol.

The TiO₂ nanoparticles prepared above were then used for the preparation of Cu-TiO₂ nanocomposites. In a typical reaction, a calculated amount of copper acetate and TiO₂ nanoparticles (at a TiO₂:Cu molar ratio of 4:1) was dispersed in THF. NaBH₄ dissolved in a small amount of water was added dropwise under vigorous stirring and N₂ protection, where the color of the solution was found to change quickly from blue to dark brown, signifying the formation of copper nanoparticles. After one hour of magnetic stirring, the solution was dried and the solids were washed with a copious amount of methanol to remove reaction byproducts or excess ligands, affording purified nanocomposites that were denoted as Cu/TiO₂.

CuHC10/TiO₂ was prepared in a similar fashion except that a 10-fold molar excess of 1-decyne was added to the solution prior to the addition of NaBH₄.

2.3 Characterizations

The morphology and sizes of the nanoparticles were characterized by transmission electron microscopic studies (TEM, Philips CM300 at 300 kV). X-ray diffraction (XRD) measurements were performed with a Rigaku Miniflex powder diffractometer using Cu Kα radiation with a Ni filter (λ = 0.154059 nm at 30 kV and 15 mA) which features a detection limit of 0.04°. X-ray photoelectron spectra (XPS) were recorded with a PHI 5400/XPS instrument equipped with an Al Kα source operated at 350 W and 10⁻⁹ Torr. Silicon wafers were sputtered by argon ions to remove carbon from the background and used as substrates. The Si2p peak (99.15 eV) was used as the reference, and deconvolution of the XPS spectra was carried out by using XPSPEAK 4.1.

2.4 Electrochemistry

Electrochemical tests were carried out in a standard three-electrode cell connected to a CHI 710C electrochemical work station, with a Pt foil counter electrode and a Hg/HgO (0.1M NaOH aq.) reference electrode. The working electrode is a rotating (platinum) ring-(glassy-carbon) disk electrode (RRDE). To prepare catalyst solutions for oxygen reduction tests, typically 0.4 mg of the nanocomposite catalysts and 1.6 mg of carbon black with 4 μL of Nafion were ultrasonically mixed in 0.4 mL of ethanol. Then 15 μL of the catalyst inks was slowly dropcast onto the glassy-carbon disk electrode of the RRDE and dried under gentle N₂ (corresponding to a loading of 15 μg in total including TiO₂ and copper nanoparticles). When the electrode was dried, a dilute Nafion solution (0.1 wt.%, 3 μL) was added onto it, prior to being immersed into electrolyte solutions for electrochemical measurements.

3. Results and discussion

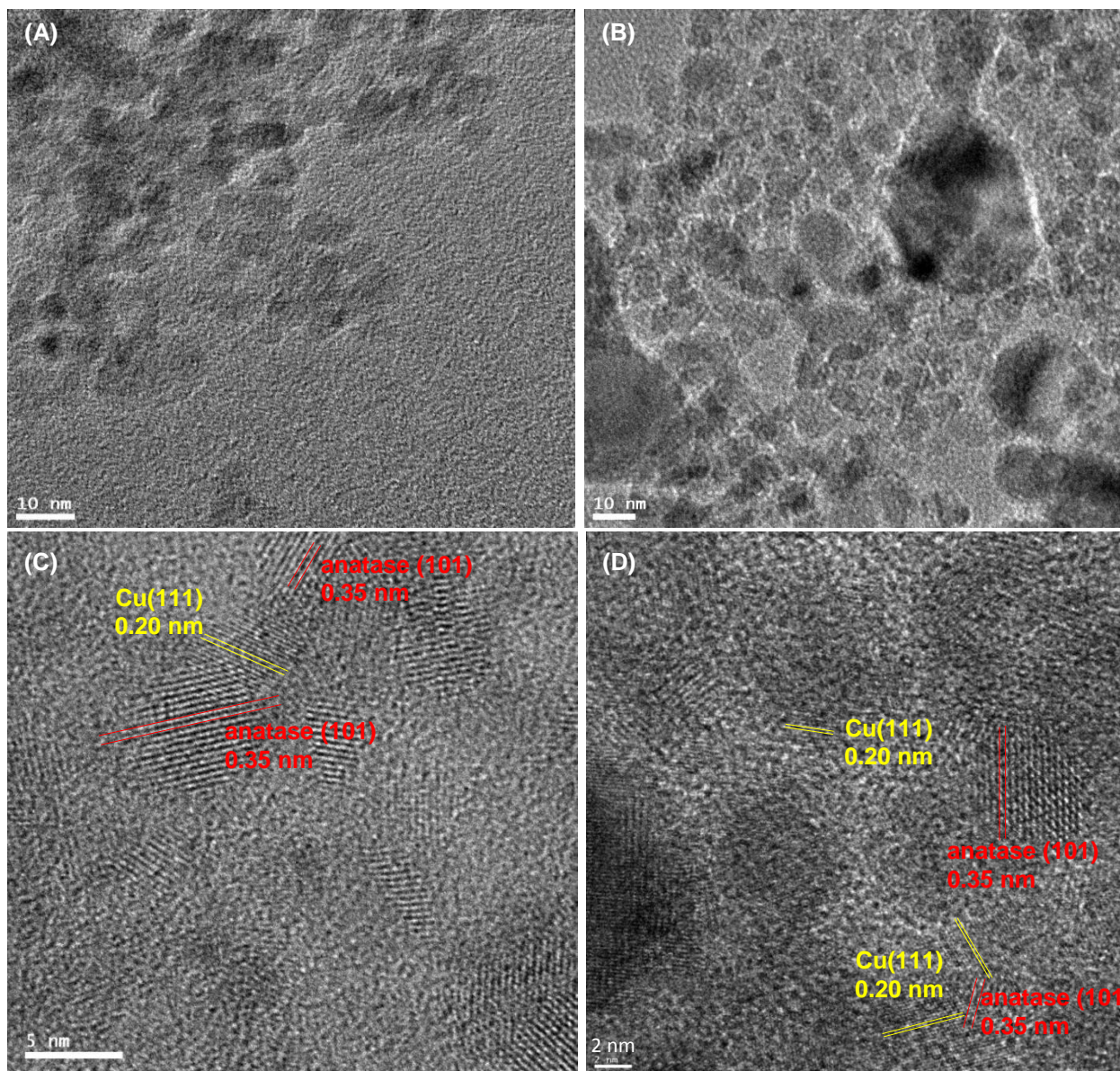


Figure 1. Representative TEM micrographs of (A and C) Cu/TiO₂ and (B and D) CuHC10/TiO₂ nanoparticles. Scale bars are 10 nm in panels (A) and (B), 5 nm in (C) and 2 nm in (D). Yellow lines highlight the Cu(111) lattice fringes whereas red lines are for anatase TiO₂ (101).

Figure 1 depicts the representative TEM micrographs of the (A) Cu/TiO₂ and (B) CuHC10/TiO₂ nanoparticles. In both images, individual nanoparticles can be identified but with rather apparent agglomeration, especially with the Cu/TiO₂ samples in panel (A); and the size of the hybrid nanoparticles range from 5 to 15 nm in diameter. High-resolution imaging in panels (C) and (D) shows that indeed copper nanoparticles were grown on TiO₂ nanocolloid surfaces, forming nanocomposites, as manifested by the well-defined lattice fringes for Cu(111) and anatase TiO₂ (101) that were in intimate contact and featured an interlayer spacing of 0.20 and 0.35 nm, respectively.^{31, 32} In addition, the Cu nanocrystals can be seen to be around 2 nm whereas TiO₂ was markedly larger at 5 nm and above.

The structures of the nanocomposites were then characterized by XRD measurements. Figure 2 depicts the

XRD patterns of the TiO₂ (black curve), Cu/TiO₂ (red curve) and CuHC10/TiO₂ (green curve) nanoparticles, which all exhibited a series of diffraction peaks (labelled by @) at 25.3°, 37.9°, 48.0°, 54.5° and 62.8°, corresponding to the (101), (004), (200), (213), and (116) crystalline planes of anatase TiO₂ (JCPDS 75-1537), respectively. Furthermore, based on the width of these diffraction peaks, the average size (τ) of the TiO₂ nanocrystallites might be quantitatively estimated by using the Debye-Scherrer equation, $\tau = K\lambda/\beta\cos\theta$, where K is a dimensionless shape factor with a value of 0.9, λ is the X-ray wavelength (1.54059 Å for Cu K α), and β is the full width at half-maximum (fwhm) of a selected diffraction peak. On the basis of the TiO₂ (101) peaks, the size (τ) was quantified and actually very consistent among the three samples, 5.1 nm for the as-prepared TiO₂, 4.1 nm for Cu/TiO₂, and 5.5 nm for CuHC10/TiO₂, in good agreement with the TEM results

presented in Figure 1. Note that no Cu diffraction patterns can be identified in XRD measurements, probably because of the small size and low loading of the Cu nanocrystals[†] (Figure 1).

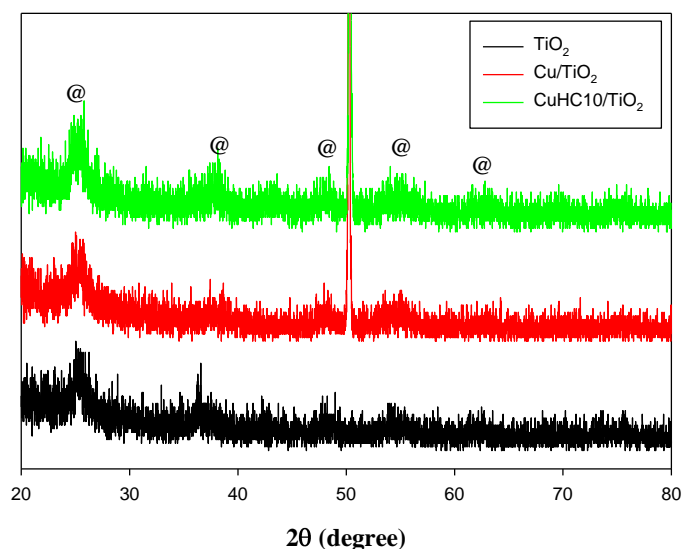
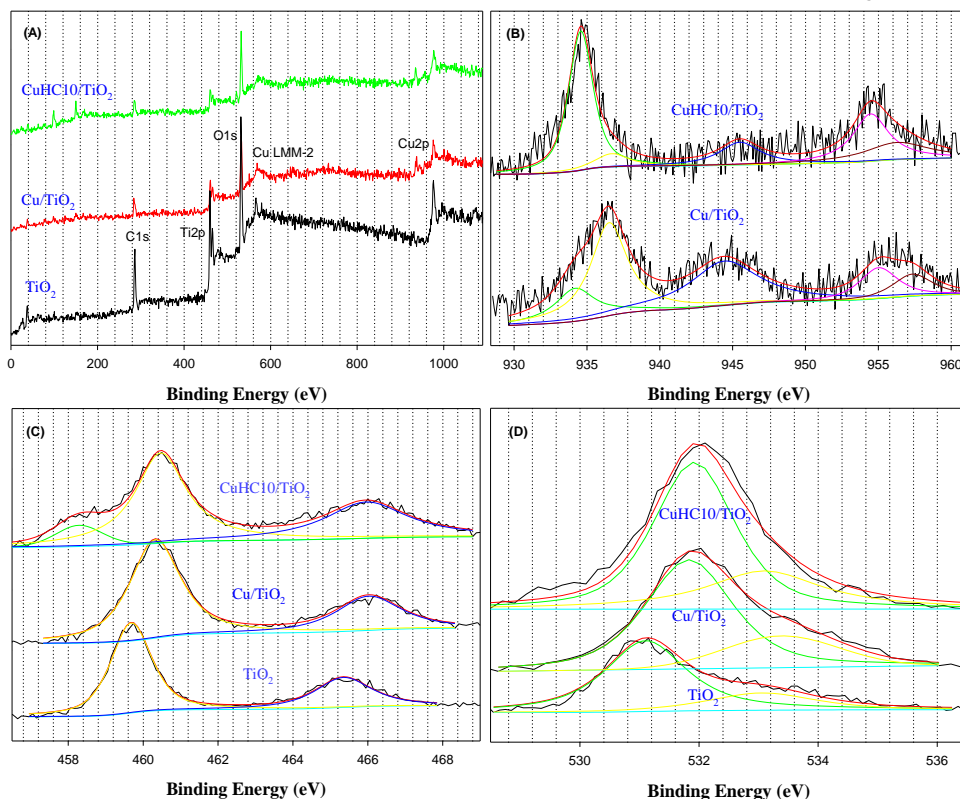


Figure 2. XRD patterns of TiO₂ (black curve), Cu/TiO₂ (red curve) and CuHC10/TiO₂ (green curve) nanoparticles. Legends “@” highlight the diffraction peaks of anatase TiO₂.

samples (black curve, where the broad peak centered at 3300 cm⁻¹ was likely due to residual water). This suggests efficient breaking of the ≡C–H bond after the alkyne ligands were adsorbed onto the copper nanoparticle surface. In addition, the absence of this vibration band also indicates that the CuHC10/TiO₂ nanocomposites were free of excessive alkyne ligands. Additionally the C≡C vibrational stretch can be identified at 2120 cm⁻¹ for monomeric 1-decyne ligands; yet this band red-shifted to 1720 cm⁻¹ for the CuHC10/TiO₂ nanoparticles. This phenomena may be explained by the cleavage of the ≡C–H bond and the formation of Cu–C≡ interfacial linkages, where the conjugated metal-ligand bonds led to effective intraparticle charge delocalization between the particle-bound acetylene moieties and hence a decreasing bonding order of the C≡C moieties, as observed in previous studies.⁸

The chemical nature of the hybrid nanoparticles was then examined by XPS measurements. Figure 3 (A) shows the full survey spectra of TiO₂, Cu/TiO₂ and CuHC10/TiO₂ composite nanoparticles. In TiO₂ nanocolloids, four major peaks can be readily identified at 286 eV (C1s), 460 eV (Ti2p), 536 eV (O1s) and 976 eV (oxygen Auger). For Cu/TiO₂ and CuHC10/TiO₂ hybrid nanoparticles, additional peaks emerged, and the peak at ca. 935 eV might be ascribed to Cu2p electrons, whereas the



peak at around 570 eV most likely arose from the Cu LMM-2 auger transitions of Cu₂O.³³ This suggests the successful deposition of copper on the TiO₂ surfaces where cuprous oxide (Cu₂O) likely formed within the nanoparticles. Furthermore, based on the corresponding integrated peak areas, the Cu/Ti atomic ratio was found to be rather consistent between the two hybrid nanoparticles, 14.7% for Cu/TiO₂ and 12.6% for CuHC10/TiO₂.

Figure 3. XPS full survey spectra (A) and high-resolution scans of the (B) Cu2p, (C) Ti2p and (D) O1s electrons of TiO₂, Cu/TiO₂ and CuHC10/TiO₂ nanoparticles. Black curves are experimental data and color curves are deconvolution fits.

The successful passivation of the copper nanoparticles by the decyne ligands in CuHC10/TiO₂ is manifested in FTIR measurements, as shown in Figure S1. It can be seen that the ≡C–H vibrational stretch at 3312 cm⁻¹ and bending vibration at 628 cm⁻¹ were well-defined for the monomeric ligands of 1-decyne (red curve); yet both vanished with the nanoparticle

High-resolution scans of the Cu2p electrons in Cu/TiO₂ and CuHC10/TiO₂ are depicted in panel (B), where the black curves are the experimental data and colored curves are deconvolution fits. For both samples deconvolution yields two pairs of doublets for the Cu2p electrons. For Cu/TiO₂, the first doublet can be identified at 934.3 and 955.1 eV, which might be ascribed to metallic Cu2p electrons, and the second doublet at 936.8 and 957.5 eV most likely arising from CuO. Similar behaviors can be seen with the CuHC10/TiO₂ hybrids, where metallic Cu2p can be

found at 934.6 and 954.5 eV and CuO at 937.1 and 956.4 eV (note that the binding energies of the Cu2p electrons for Cu(0) and Cu(I) are only 0.1 eV apart, thus the data likely reflected the combined contributions from both species).³⁴ One can see that the CuO concentration in Cu/TiO₂ was significantly greater than that in CuHC10/TiO₂. In fact, based on the integrated peak areas, the ratio of Cu(II) over the entire copper species in the nanoparticles was estimated to be 48.2% for Cu/TiO₂ and 13.0% for CuHC10/TiO₂.

The formation of cupric oxide (CuO) in the nanoparticles is also manifested by the satellite between the twin peaks.³⁵ Note that the appearance of the satellite peak has been largely ascribed to the shake-up effect where the outgoing electron interacts with a valence electron and excites it to a higher energy level.³⁵ Cu(II) components exhibit a vacant 3d orbital while Cu(I) or Cu(0) features a 3d¹⁰ electronic configuration with 4s being the lowest-energy empty orbital. Therefore, one can see from panel (B) that the higher Cu(II) concentration in Cu/TiO₂ nanoparticles is consistent with the satellite peak (943.89 eV) that was somewhat red-shifted as compared to that (944.96 eV) of CuHC10/TiO₂ nanoparticles; and the peak intensity of the former is markedly greater than that of the latter, likely because of effective protection of the nanoparticle surface by the decyne ligands in CuHC10/TiO₂.

High-resolution scans of the Ti2p electrons of TiO₂, Cu/TiO₂ and CuHC10/TiO₂ are shown in panel (C). All three nanoparticle samples yield a doublet that was consistent with those of TiO₂ colloids reported previously,³⁶ 459.7 and 465.4 eV for TiO₂, 460.3 and 466.0 eV for Cu/TiO₂, and 460.5 and 466.0 eV for CuHC10/TiO₂. In addition, it is apparent that the CuHC10/TiO₂ nanoparticles show an extra peak at a somewhat lower energy (458.2 eV) than that of Ti(IV) (460.5 eV), which might be assigned to Ti(III),³⁷ and from the integrated peak areas the relative ratio of Ti(III) over Ti(IV) was estimated to be 19.8%. In contrast, no Ti(III) was observed with Cu/TiO₂, which was likely due to the high concentration of CuO that impeded the reduction of Ti(IV) to Ti(III).

Panel (D) depicts the corresponding high-resolution scans of the O1s electrons. The O1s spectra of all three samples can be deconvoluted into a main peak at 531 eV and a shoulder at a higher binding energy of about 533 eV. The main peaks are consistent with those reported in the literature for bulk oxides, and the binding energy of the shoulders is in agreement with that of surface OH species.³⁸ The relative amounts of surface OH species can be quantified on the basis of the corresponding integrated peak areas: 29.6% for TiO₂, 30.2% for Cu/TiO₂, and 44.1% for CuHC10/TiO₂. It has been reported that hydroxyl groups are formed on TiO₂ surfaces during water dissociation with oxygen vacancies as the active sites.³⁹ In the present study, whereas the concentration of surface oxygen vacancies was rather comparable between TiO₂ and Cu/TiO₂, it was markedly higher in CuHC10/TiO₂. This is consistent with the formation of Ti(III) species in the CuHC10/TiO₂ nanoparticles as observed above that likely played an important role in enhancing the ORR activity, as detailed below.

Interestingly, both the Cu/TiO₂ and CuHC10/TiO₂ nanocomposites synthesized above exhibited apparent electrocatalytic activities towards oxygen reduction in alkaline media. Figure 4 shows the steady-state cyclic voltammograms of a glassy-carbon electrode (out of a platinum ring-glassy carbon disk electrode) modified with a calculated amount of Cu/TiO₂ and CuHC10/TiO₂ in a N₂-saturated 0.1 M NaOH solution. There are several aspects that warrant attention here. First, TiO₂ nanoparticles exhibited only featureless double-layer charging currents (black curve), primarily because of the large bandgap of TiO₂ and hence low electronic conductivity within the potential range of +0.1 to +1.1 V.⁴⁰ Second, the double-layer charging currents were markedly enhanced when the electrode was modified with Cu/TiO₂ (red curve) or CuHC10/TiO₂ (green curve) nanoparticles. For instance, the double-layer charging currents at +0.40 V increased in the order of 1(TiO₂):1.35(Cu/TiO₂):2.70(CuHC10/TiO₂), signifying enhanced dispersion of the hybrid nanoparticles on the electrode surface. Additional contributions might arise from the enhanced conductivity of CuHC10/TiO₂ by defective Ti(III) species (Figure 3).²⁹ Furthermore, two anodic peaks emerged at around +0.55 V and +0.84 V (vs RHE), where the former might be ascribed to the formation of a monolayer of Cu₂O while the latter to the formation of a thick multilayer film of CuO, and concurrently, a cathodic peak can be seen at around +0.66 V, likely arising from the partial reduction of CuO to Cu₂O.⁴¹ Similar voltammetric features have also been observed in a previous study with decyne-capped copper nanoparticles.¹⁹ Finally, the fact that these voltammetric peak currents were only slightly greater for CuHC10/TiO₂ than for Cu/TiO₂ suggests that electrochemically accessible surface areas of copper nanoparticles were rather comparable in both hybrid nanoparticles.

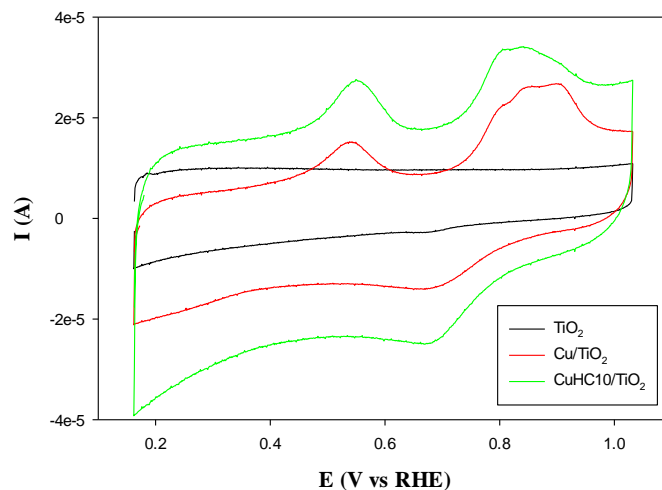


Figure 4. Cyclic voltammograms of a glassy carbon-disk electrode modified with 15 μg of TiO₂ (black curve), Cu/TiO₂ (red curve) or CuHC10/TiO₂ (green curve) nanoparticles in a nitrogen-saturated 0.1M NaOH solution. Potential scan rate 10 mV/s.

Figure 5 depicts the RRDE voltammograms of the same electrodes in an O₂-saturated 0.1 M NaOH solution at different rotation rates. For all three electrodes, it can be seen that

significant cathodic currents started to emerge at sufficiently negative potentials indicating apparent electrocatalytic activity towards oxygen reduction. For (A) TiO_2 and (B) Cu/TiO_2 catalysts, the onset potential was identified at around +0.74 V, and for (C) $\text{CuHC10}/\text{TiO}_2$ nanoparticles it was somewhat more positive at +0.75 V. In addition, with the $\text{CuHC10}/\text{TiO}_2$ and Cu/TiO_2 nanocomposites the limiting currents were significantly increased, as compared to that of TiO_2 alone. For instance, for TiO_2 nanoparticle catalysts alone, the limiting current at 2500 rpm was only about 0.87 mA, yet with Cu/TiO_2 catalyst the limiting current almost doubled to 1.54 mA, and with $\text{CuHC10}/\text{TiO}_2$ to 1.50 mA.

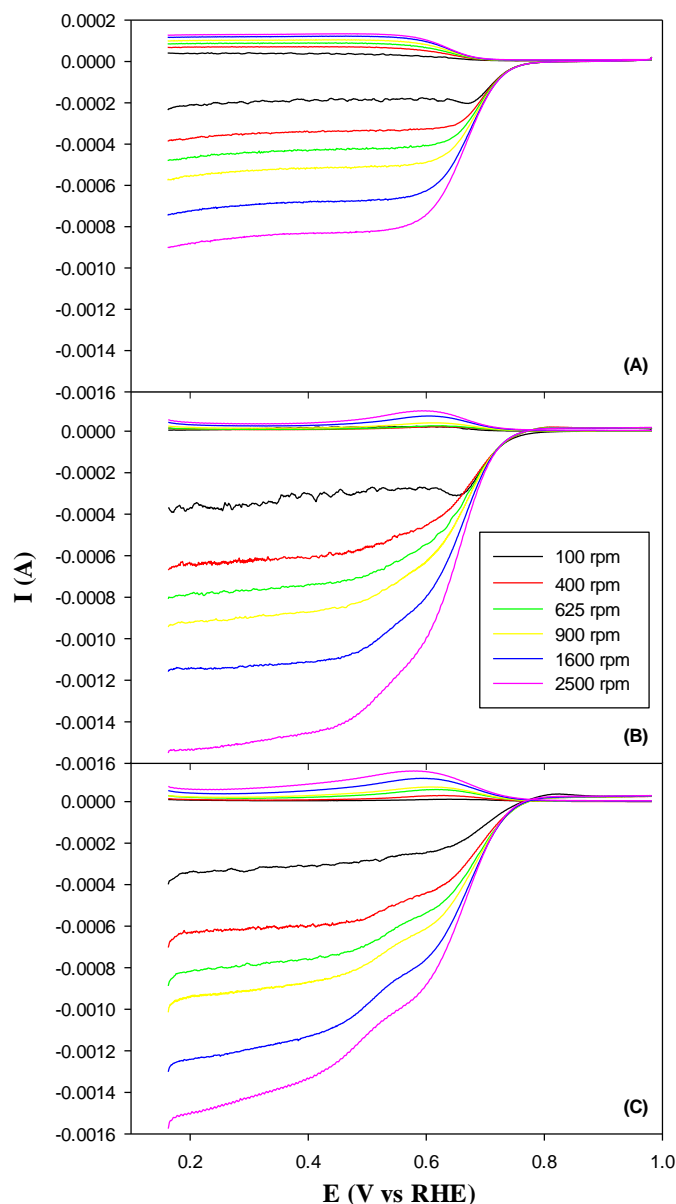


Figure 5. RRDE voltammograms of a platinum ring-glassy-carbon disk electrode with the disk modified with (A) TiO_2 , (B) Cu/TiO_2 , and (C) $\text{CuHC10}/\text{TiO}_2$ nanoparticles in an oxygen-saturated 0.1 M NaOH solution. Nanoparticle loading is all 15 μg . Electrode rotation rates are specified in the figure legends. Ring currents are collected by setting the ring potential at +1.3 V vs RHE.

Furthermore, the voltammetric currents collected at the ring electrode, where the potential was set at +1.3 V, were about an order of magnitude lower than the corresponding disk currents, signifying that only a minimal amount of peroxide species were produced during oxygen reduction. From the ratio of the ring current (I_R) and disk current (I_D), the number of electron transfer (n) during oxygen reduction can be estimated by $n = 4I_D/(I_D + I_R/N)$, with N being the collection efficiency (37%), as depicted in Figure 6. It can be seen that for TiO_2 , n increased from zero to 2 rapidly with the electrode potential swept from +0.76 V to +0.70 V, while for Cu/TiO_2 and $\text{CuHC10}/\text{TiO}_2$ the increase was much more drastic. At more negative potentials the n values increased accordingly and finally reached 2.69 for TiO_2 , 3.74 for Cu/TiO_2 and 3.69 for $\text{CuHC10}/\text{TiO}_2$, and the corresponding fractions of peroxide species in the reaction products were estimated to be 65.5%, 13.0% and 15.5%, respectively. It is well known that oxygen reduction in aqueous solutions typically occurs through two major pathways: the direct four-electron reduction pathway from O_2 to OH^- ($n = 4$) and the two-electron reduction pathway from O_2 to H_2O_2 ($n = 2$). This means that at TiO_2 alone, the oxygen reduction was dominated by the 2-electron pathway, while the 4-electron reduction pathway was the dominant one for Cu/TiO_2 and $\text{CuHC10}/\text{TiO}_2$.

Further insights into the electron-transfer kinetics of oxygen reduction were revealed by Koutecky-Levich analysis, as the RRDE voltammetric currents include both kinetic (I_k) and diffusion (I_d) controlled contributions,⁴²

$$\frac{1}{I_D} = \frac{1}{I_k} + \frac{1}{I_d} = \frac{1}{I_k} + \frac{1}{B\omega^{1/2}} \quad (1a)$$

$$B = 0.62nFAC_0D_0^{2/3}\nu^{-1/6} \quad (1b)$$

$$I_k = nAFkC_0 \quad (1c)$$

where ω is the electrode rotation rate, n is the overall number of electron transfer, F is Faraday constant, C_0 is the bulk concentration of O_2 dissolved in the electrolyte, D_0 is the diffusion coefficient of O_2 , and ν is the kinetic viscosity of the electrolyte.⁴³ Figure S2 depicts the Koutecky-Levich plots (I_D^{-1} vs $\omega^{-1/2}$) of (A) TiO_2 , (B) Cu/TiO_2 and (C) $\text{CuHC10}/\text{TiO}_2$ nanoparticles within the potential range of +0.76 to +0.60 V. One can see that all experimental data exhibited good linearity and the slopes of each nanoparticle catalyst remained approximately constant. The linearity and parallelism of the plots are usually taken as a strong indication of a first-order reaction with respect to dissolved oxygen. From the linear regressions in Figure S2, the kinetic currents (I_k) could also be quantified from the y-axis intercepts. This is manifested in the Tafel plot (inset to Figure 6), where it can be seen that within the low overpotential region ($E > +0.66$ V), the kinetic currents increase in the order of $\text{TiO}_2 < \text{Cu}/\text{TiO}_2 < \text{CuHC10}/\text{TiO}_2$. For instance, at +0.70 V, the kinetic current density (J_k) was 8.83 A/m^2 for TiO_2 , 9.18 A/m^2 for Cu/TiO_2 and 12.38 A/m^2 for $\text{CuHC10}/\text{TiO}_2$, indicating that $\text{CuHC10}/\text{TiO}_2$ stood out as the best catalyst among the series (one may note that at high overpotentials ($E < +0.66$ V), the J_k values were actually higher for Cu/TiO_2 than for $\text{CuHC10}/\text{TiO}_2$. This may be ascribed to the much higher concentration of CuO in Cu/TiO_2 that was

electrochemically reduced to Cu_2O at these potentials (Figure 4) as Cu_2O was known to be active in ORR, *vide infra*).

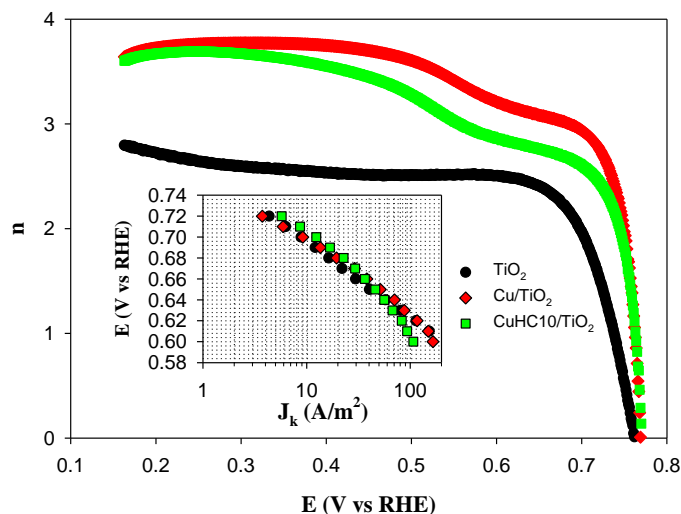


Figure 6. Variation of the number of electron transfer (n) in oxygen reduction with electrode potential for TiO_2 (black curves), Cu/TiO_2 (red curves) and $\text{CuHC10}/\text{TiO}_2$ (green curves) nanoparticles. Symbols were experimental data calculated from the RRDE voltammograms at 1600 rpm in Figure 5. Inset shows the corresponding Tafel plots. Data are acquired from linear regressions of the Koutecky-Levich plots in Figure S2. Electrode geometrical surface area was used to calculate the current density.

The slope of the Tafel plot can also be used to gain further insights into the dynamics of oxygen reduction reaction. For oxygen electroreduction at nanoparticle catalyst surfaces, the Tafel slopes are typically found at 60 mV/dec or 120 mV/dec, where the former corresponds to a pseudo two-electron reaction as the rate determining step, and in the latter, ORR is presumed to be limited by the first-electron reduction of oxygen.⁴⁴ In the present study, linear regressions of the Tafel plots yield a slope of 70.5 mV/dec for TiO_2 , suggesting that oxygen reduction reaction was largely limited by a pseudo two-electron process (corresponding to a relatively large fraction of peroxide species in the reduction products). For $\text{CuHC10}/\text{TiO}_2$, the Tafel plot actually includes two linear segments with different slopes. At low current densities ($E > +0.66$ V), the Tafel slope was about 58.5 mV/dec, implying the pseudo two-electron reaction as the rate-determining step in the low overpotential region. At high current densities ($E < +0.66$ V) the Tafel slope increased to 118.5 mV/dec, consistent with the first-electron reduction of oxygen as the rate-determining step (implying a facile O–O bond breaking step at high overpotentials). Similar behaviors can be seen with the Cu/TiO_2 sample with the two slopes of 56.7 mV/dec and 90.2 mV/dec, respectively. Dual Tafel slopes in ORR have been observed previously with Pt-based electrocatalysts,⁴⁵ and accounted for by a double-trap kinetic model,⁴⁶ where the turning point (+0.66 V in the present study) reflects the equilibrium potential for the dynamic transition between surface-adsorbed reaction intermediates like O^* and HO^* . Note that this potential coincided with the formation of Cu_2O for both $\text{CuHC10}/\text{TiO}_2$ and Cu/TiO_2 , as manifested in Figure 4, and Cu_2O has been suggested to serve as effective active sites for ORR by donating electrons to oxygen.¹⁹

Additional contributions may arise from the relatively hydrophilic surfaces of $\text{CuHC10}/\text{TiO}_2$ and Cu/TiO_2 hybrid nanoparticles that facilitated water dissociation and formation of surface-adsorbed hydroxyl species, as evidenced in XPS measurements (Figure 3), where fast interactive effusion of H-adatoms over hydrated surfaces has been believed to enhance electrocatalytic activity.^{47, 48} Furthermore, the Ti^{3+} defects in $\text{CuHC10}/\text{TiO}_2$ (Figure 3) might also help enhance the adsorption and eventual reduction of oxygen on copper by interfacial charge transfer.²⁹ All these led to a much enhanced ORR activity of $\text{CuHC10}/\text{TiO}_2$ as compared to those of Cu/TiO_2 and TiO_2 .

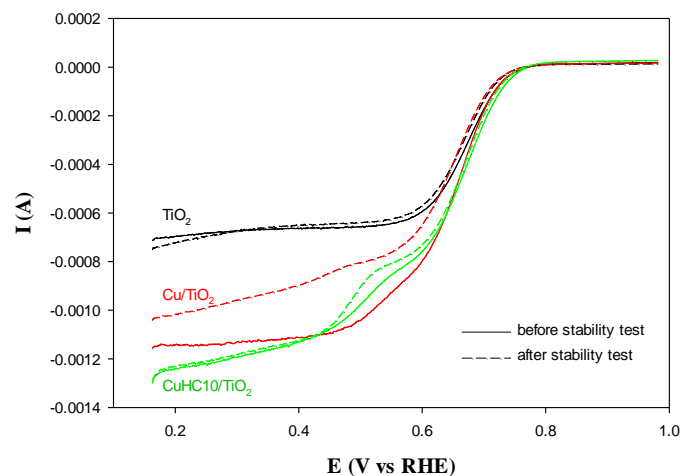


Figure 7. Polarization curves for oxygen reduction catalyzed by TiO_2 (A), Cu/TiO_2 (B), and $\text{CuHC10}/\text{TiO}_2$ (C) before (solid curves) and after (dashed curves) 4000 potential cycles with a potential scan rate of 50 mV/s from +0.6 to 1.1 V in O_2 saturated 0.1M NaOH solution. Electrode rotation rate: 1600 rpm. Other experimental conditions were the same as in Figure 5.

Durability is another important parameter in the evaluation of nanoparticle catalytic performance. In the present study, durability tests were performed in oxygen-saturated 0.1 M NaOH at a potential sweep rate of 50 mV/s between +0.6 V and +1.1 V for 4000 cycles.⁴⁹ The RDE polarization curves before (solid curves) and after (dashed curves) durability tests were depicted in Figure 7. It can be seen that for TiO_2 nanoparticles alone (black curves), the polarization curve showed a cathodic shift of about 10 mV with virtually no change of the diffusion limiting current. For the Cu/TiO_2 nanoparticles (red curves), the polarization curve was negatively shifted by as much as 30 mV, along with about 9% diminishment of the limiting current. In sharp contrast, no apparent change was observed with $\text{CuHC10}/\text{TiO}_2$ (green curves), indicating markedly enhanced stability of the hybrid nanoparticles that was likely due to the decyne capping ligands.

One may note that the electrocatalytic performance of these Cu/TiO_2 and $\text{CuHC10}/\text{TiO}_2$ hybrid nanoparticles remains subpar as compared to those of Pt or Pd-based nanoparticle catalysts which typically exhibit an onset potentials more positive than +0.90 V and $n \approx 4.0$.^{7, 8, 50, 51} Yet, the activity is actually rather comparable to that of Au- TiO_2 nanocomposites (10 – 50 nm in diameter, $n = 3.7$ at +0.60 V, onset potential +0.88 V),⁵² and markedly better than that observed previously

with alkyne-capped copper nanoparticles.¹⁹ In the latter, the nanoparticles (4 – 6 nm in diameter) were also capped with 1-decyne, and carbon black rather than TiO₂ nanoparticles was used as the catalytic supports.¹⁹ Without the strong metal-support interactions from TiO₂, however, peroxide species constituted a major portion of the oxygen reduction products ($n = 2.5 - 2.7$ within the potential range of +0.70 to +0.40 V) and the corresponding limiting current at 2500 rpm was only 0.8 mA. This signifies the importance of TiO₂ in the activation of water and formation of surface adsorbed hydroxyl species for oxygen reduction in the so-called primary oxide spillover mechanism. It should be emphasized that the ORR activity of copper-based bulk electrodes is rather marginal.^{16-18, 53} For instance, in the previous studies with a polycrystalline Cu or CuNi electrode,^{16, 17} the onset potentials for oxygen reduction were found to be around +0.36 V (vs RHE) in a borax buffer solution; and even more negative onset potentials were observed with single-crystalline Cu(100) and Cu(111) electrodes in H₂SO₄ at about 0 V (vs RHE).^{18, 53} These are far more negative than those observed above with the hybrid nanoparticles.

4. Conclusion

In this study, copper nanoparticles with or without 1-decyne capping ligands were grown onto TiO₂ nanocolloid surfaces. The structures of the resulting nanocomposites were then subject to a wide range of characterizations. TEM measurements showed that the TiO₂ colloids were largely of anatase phase, and the close proximity of the TiO₂(101) and Cu(111) lattice fringes suggested intimate contacts between the two components. Further structural details were unravelled in XRD measurements where the diffraction features of anatase TiO₂ were clearly defined whereas those of copper were not resolved, likely because of the small size and low loading of copper in the composites. XPS measurements suggested the formation of CuO in both hybrid nanoparticles, with a much higher concentration in Cu/TiO₂ than in CuHC10/TiO₂, most probably because of the decyne capping ligands in the latter. Interestingly, Ti³⁺ species were identified in CuHC10/TiO₂ nanoparticles but not in Cu/TiO₂, which may, at least in part, account for the enhanced ORR activity of the former. Electrochemical studies indicated that electrocatalytic activity in oxygen reduction in alkaline media was significantly improved after copper species were chemically grown onto TiO₂ nanoparticles, as manifested in the increase in number of electrons transferred from about 2.69 up to 3.74, an apparent anodic shift of the onset potential, a rather drastic increase of the kinetic current density and remarkable long-term stability. Among the series, the best performance was observed with CuHC10 nanoparticles, which was ascribed to the activation of water by TiO₂ and the formation of surface-adsorbed hydroxyl species facilitated by defective Ti³⁺ sites. Taken together, the results presented herein indicates that the synergistic interactions between non-precious metals and metal oxides might be exploited for the development of effective catalysts

based on earth-abundant and cost-effective materials for fuel cell electrochemistry.

Acknowledgements

This work was supported in part by the National Science Foundation (CHE – 1012258, CHE – 1265635, and DMR – 1409396). TEM and XPS work was carried out at the National Center for Electron Microscopy and Molecular Foundry, Lawrence Berkeley National Laboratory as part of a user project.

Notes and references

Department of Chemistry and Biochemistry, University of California, 1156 High Street, Santa Cruz, California 95064, USA. * E-mail: shaowei@ucsc.edu

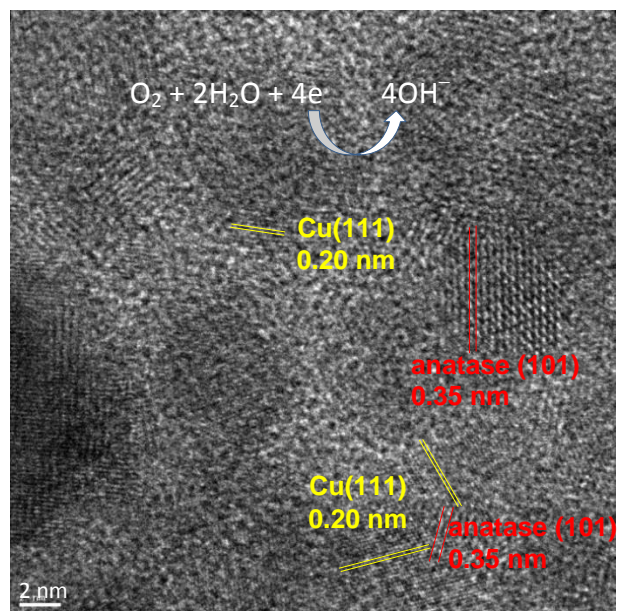
† Whereas the sharp peak at 50.4° appeared to be consistent with diffraction from the Cu(200) crystalline planes, a much more intense diffraction for Cu(111) should have emerged at 43.4°. This was not observed in Figure 2. Thus it is unlikely that the sharp peak at 50.4° arose from copper nanoparticles. Its origin is unknown at this point.

Electronic Supplementary Information (ESI) available: FTIR spectra and Koutecky-Levich plots. See DOI: 10.1039/b000000x/

1. E. Proietti, F. Jaouen, M. Lefèvre, N. Larouche, J. Tian, J. Herranz and J.-P. Dodelet, *Nat Commun*, 2011, 2, 416.
2. F. T. Wagner, B. Lakshmanan and M. F. Mathias, *J Phys Chem Lett*, 2010, 1, 2204-2219.
3. R. Rizo, E. Herrero and J. M. Feliu, *Phys Chem Chem Phys*, 2013, 15, 15416-15425.
4. H. H. Wang, Z. Y. Zhou, Q. A. Yuan, N. Tian and S. G. Sun, *Chem Commun*, 2011, 47, 3407-3409.
5. J. Zhang, K. Sasaki, E. Sutter and R. R. Adzic, *Science*, 2007, 315, 220-222.
6. Z. Y. Zhou, X. W. Kang, Y. Song and S. W. Chen, *Chem Commun*, 2012, 48, 3391-3393.
7. Z. Y. Zhou, X. W. Kang, Y. Song and S. W. Chen, *J Phys Chem C*, 2012, 116, 10592-10598.
8. K. Liu, X. W. Kang, Z. Y. Zhou, Y. Song, L. J. Lee, D. Tian and S. W. Chen, *J Electroanal Chem*, 2013, 688, 143-150.
9. R. Bashyam and P. Zelenay, *Nature*, 2006, 443, 63-66.
10. M. Lefevre, E. Proietti, F. Jaouen and J. P. Dodelet, *Science*, 2009, 324, 71-74.
11. G. Wu, K. L. More, C. M. Johnston and P. Zelenay, *Science*, 2011, 332, 443-447.
12. S. Wang, D. Yu and L. Dai, *J Am Chem Soc*, 2011, 133, 5182-5185.
13. S. Koh and P. Strasser, *J Am Chem Soc*, 2007, 129, 12624-12625.
14. N. N. Kariuki, X. Wang, J. R. Mawdsley, M. S. Ferrandon, S. G. Niyogi, J. T. Vaughney and D. J. Myers, *Chem Mater*, 2010, 22, 4144-4152.
15. H. H. Li, C. H. Cui, S. Zhao, H. B. Yao, M. R. Gao, F. J. Fan and S. H. Yu, *Adv Energy Mater*, 2012, 2, 1182-1187.
16. M. V. Vazquez, S. R. Desanchez, E. J. Calvo and D. J. Schiffrin, *J Electroanal Chem*, 1994, 374, 189-197.
17. S. Cere, M. Vazquez, S. R. de Sanchez and D. J. Schiffrin, *J Electroanal Chem*, 2001, 505, 118-124.
18. T. Jiang and G. M. Brisard, *Electrochim Acta*, 2007, 52, 4487-4496.
19. Y. S. K. Liu, S. Chen, *J. Power. Sources*, 2014, 268, 469-475.
20. T. J. Schmidt, H. A. Gasteiger, G. D. Stab, P. M. Urban, D. M. Kolb and R. J. Behm, *J Electrochem Soc*, 1998, 145, 2354-2358.
21. M. K. Min, J. H. Cho, K. W. Cho and H. Kim, *Electrochim Acta*, 2000, 45, 4211-4217.
22. N. Rajalakshmi, N. Lakshmi and K. Dhathathreyan, *Int J Hydrogen Energy*, 2008, 33, 7521-7526.
23. B. E. Hayden, D. V. Malevich and D. Pletcher, *Electrochem Commun*, 2001, 3, 395-399.

24. M. Wang, D. J. Guo and H. L. Li, *J Solid State Chem*, 2005, 178, 1996-2000.
25. J. L. Shim, C. R.; Lee, H. K.; Lee, J. S.; Cairns, E. J. , *J. Power Sources*, 2001, 102, 172.
26. S. Shanmugam and A. Gedanken, *J Phys Chem C*, 2009, 113, 18707-18712.
27. S.-Y. Huang, P. Ganesan and B. N. Popov, *ACS Catal*, 2012, 2, 825-831.
28. M. M. Jaksic, G. A. Botton, G. D. Papakonstantinou, F. H. Nan and J. M. Jaksic, *J Phys Chem C*, 2014, 118, 8723-8746.
29. T. L. Thompson and J. T. Yates, *Chem Rev*, 2006, 106, 4428-4453.
30. D. C. Pan, N. N. Zhao, Q. Wang, S. C. Jiang, X. L. Ji and L. J. An, *Adv Mater*, 2005, 17, 1991-1995.
31. R. Ramanathan, M. R. Field, A. P. O'Mullane, P. M. Smooker, S. K. Bhargava and V. Bansal, *Nanoscale*, 2013, 5, 2300-2306.
32. Q. Zhu, J. S. Qian, H. Pan, L. Tu and X. F. Zhou, *Nanotechnology*, 2011, 22.
33. T. Ghodselahi, M. A. Vesaghi, A. Shafiekhani, A. Baghizadeh and M. Lameii, *Appl Surf Sci*, 2008, 255, 2730-2734.
34. C. D. Wagner, W. M. Riggs, L. E. Davis, J. F. Moulder and G. E. Muilenberg, *Handbook of x-ray photoelectron spectroscopy : a reference book of standard data for use in x-ray photoelectron spectroscopy*, Perkin-Elmer Corp., Eden Prairie, Minn., 1979.
35. K. S. Kim, *J. Electron. Spectrosc. Relat. Phenom.*, 1974, 3, 217-226.
36. B. Erdem, R. A. Hunsicker, G. W. Simmons, E. D. Sudol, V. L. Dimonie and M. S. El-Aasser, *Langmuir*, 2001, 17, 2664-2669.
37. S. Sodergren, H. Siegbahn, H. Rensmo, H. Lindstrom, A. Hagfeldt and S. E. Lindquist, *J Phys Chem B*, 1997, 101, 3087-3090.
38. M. Kunat, S. G. Girol, U. Burghaus and C. Woll, *J Phys Chem B*, 2003, 107, 14350-14356.
39. R. Schaub, P. Thstrup, N. Lopez, E. Lægsgaard, I. Stensgaard, J. Nørskov and F. Besenbacher, *Phys Rev Lett*, 2001, 87.
40. A. J. Nozik and R. Memming, *J Phys Chem*, 1996, 100, 13061-13078.
41. S. M. A. Elhaleem and B. G. Ateya, *J Electroanal Chem*, 1981, 117, 309-319.
42. A. J. Bard and L. R. Faulkner, *Electrochemical methods : fundamentals and applications*, Wiley, New York, 2nd edn., 2001.
43. W. Chen, J. M. Kim, S. H. Sun and S. W. Chen, *J Phys Chem C*, 2008, 112, 3891-3898.
44. J. J. Zhang, *PEM fuel cell electrocatalysts and catalyst layers : fundamentals and applications*, Springer, London, 2008.
45. G. He, Y. Song, K. Liu, A. Walter, S. Chen and S. Chen, *ACS Catal*, 2013, 3, 831-838.
46. J. X. Wang, F. A. Uribe, T. E. Springer, J. L. Zhang and R. R. Adzic, *Faraday Discuss.*, 2008, 140, 347-362.
47. J. M. Jaksic, G. D. Papakonstantinou, D. Labou, A. Siokou and M. M. Jaksic, *Adv. Phys. Chem.*, 2011, 2011, 1-22.
48. J. M. Jaksic, G. D. Papakonstantinou, D. Labou, A. Siokou and M. M. Jaksic, in *New and future developments in catalysis: hybrid materials, composites, and organocatalysts*, ed. S. L. Suib, Elsevier, Amsterdam, 2013, pp. 175-212.
49. B. Lim, M. Jiang, P. H. C. Camargo, E. C. Cho, J. Tao, X. Lu, Y. Zhu and Y. Xia, *Science*, 2009, 324, 1302-1305.
50. S. Maheswari, P. Sridhar and S. Pitchumani, *Electrochem Commun*, 2013, 26, 97-100.
51. L. Zhang, L. Y. Wang, C. M. B. Holt, T. Navessin, K. Malek, M. H. Eikerling and D. Mitlin, *J Phys Chem C*, 2010, 114, 16463-16474.
52. C. Lin, Y. Song, L. Cao and S. Chen, *ACS Appl Mater Interfaces*, 2013, 5, 13305-13311.
53. G. Brisard, N. Bertrand, P. N. Ross and N. M. Markovic, *J Electroanal Chem*, 2000, 480, 219-224.

ToC graph



ORR activity of copper nanoparticles was enhanced by defective TiO_2 that facilitated water adsorption and formation of surface hydroxyl species.